RESEARCH ARTICLE

Key Points:
- A lightning data assimilation method was developed
- Demonstrate a method to retrieve the graupel fields of convective clouds using total lightning data
- The lightning data assimilation method improves the lightning and convective precipitation short-term forecasts

Improving Lightning and Precipitation Prediction of Severe Convection Using Lightning Data Assimilation With NCAR WRF-RTFDDA

Haoliang Wang[1,2], Yubao Liu[2], William Y. Y. Cheng[2], Tianliang Zhao[1], Mei Xu[2], Yuewei Liu[2], Si Shen[2], Kristin M. Calhoun[3] (iD), and Alexandre O. Fierro[3]

[1]Collaborative Innovation Center on Forecast and Evaluation of Meteorological Disasters, Nanjing University of Information Science and Technology, Nanjing, China, [2]National Center for Atmospheric Research, Boulder, CO, USA, [3]Cooperative Institute for Mesoscale Meteorological Studies (CIMMS), NOAA/National Severe Storms Laboratory, University of Oklahoma (OU), Norman, OK, USA

Abstract In this study, a lightning data assimilation (LDA) scheme was developed and implemented in the National Center for Atmospheric Research Weather Research and Forecasting-Real-Time Four-Dimensional Data Assimilation system. In this LDA method, graupel mixing ratio (q_g) is retrieved from observed total lightning. To retrieve q_g on model grid boxes, column-integrated graupel mass is first calculated using an observation-based linear formula between graupel mass and total lightning rate. Then the graupel mass is distributed vertically according to the empirical q_g vertical profiles constructed from model simulations. Finally, a horizontal spread method is utilized to consider the existence of graupel in the adjacent regions of the lightning initiation locations. Based on the retrieved q_g fields, latent heat is adjusted to account for the latent heat releases associated with the formation of the retrieved graupel and to promote convection at the observed lightning locations, which is conceptually similar to the method developed by Fierro et al. Three severe convection cases were studied to evaluate the LDA scheme for short-term (0–6 h) lightning and precipitation forecasts. The simulation results demonstrated that the LDA was effective in improving the short-term lightning and precipitation forecasts by improving the model simulation of the q_g fields, updrafts, cold pool, and front locations. The improvements were most notable in the first 2 h, indicating a highly desired benefit of the LDA in lightning and convective precipitation nowcasting (0–2 h) applications.

1. Introduction

Thunderstorm lightning and heavy rainfall often cause property damage and threaten lives. Timely and accurate forecasts of these phenomena are critical for mitigating their impact. Lightning usually accompanies severe convective weather, as rimed ice-phase particles and strong updrafts associated with the deep convective clouds are favorable for electrification (e.g., Takahashi & Miyawaki, 2002; Macgorman et al., 2005). During the last few decades, researchers found that the total lightning rate strongly correlates with graupel contents and updrafts in convective storms (e.g., Carey et al., 2014; Deierling et al., 2008; Fierro et al., 2006; Kuhlman et al., 2006; Ribaud et al., 2016), signifying that total lightning data can be used to infer the dynamical and microphysical features of convective clouds.

Modern lightning detection systems are capable of detecting lightning over broader regions in real time with higher detection efficiency. Land-based lightning detection systems, for example, the Earth Networks Total Lightning Network (ENTLN; Liu & Heckman, 2010), and the upgraded U.S. National Lightning Detection Network (Nag et al., 2014) detects total lightning rates over the contiguous United States (CONUS). Furthermore, the Geostationary Lightning Mapper instrument aboard the recently launched Geostationary Operational Environmental Satellite-R Series can detect total lightning over CONUS and most of the Western Hemisphere (Goodman et al., 2013). The Lightning Mapping Imager instrument aboard the Feng-Yun-4 Geostationary Satellite is able to detect total lightning over China, the Western Pacific, and the Indian Ocean (Yang et al., 2017). These geostationary satellite-based lightning detection instruments further extended the range of real-time lightning detection.

The relationship between lightning activity and convective cloud properties, along with the wide detection range of the modern lightning detection systems, motivates research efforts aimed at

systematically assimilating lightning data into NWP models to generate more accurate initial conditions for forecasting severe convective weather. Previous lightning data assimilation (LDA) approaches used lightning to derive rainfall rates through empirical relationships and then modified model latent heat profiles based on the lightning derived rainfall (e.g., Alexander et al., 1999; Benjamin et al., 2004; Chang et al., 2001; Pessi & Businger, 2009). Papadopoulos et al. (2005) employed lightning to nudge the model humidity profiles toward empirical humidity profiles derived from observed soundings in thunderstorm days to encourage the convective parameterization scheme (CPS) to activate. The LDA method developed by Mansell et al. (2007) utilized total lightning data to force or suppress the triggering of the CPS. These assimilation methods were all employed in the mesoscale models with grid spacing larger than 10 km.

Following an initial idea proposed in Fierro and Reisner (2011), Fierro et al. (2012) first developed a method to assimilate lightning data at the cloud scale. They used lightning data to adjust water vapor in mixed-phase regions (0°C to −20°C) with a hyperbolic tangent-nudging function. By evaluating the short-term forecast of an outflow-dominated mesoscale convective system (MCS), which utilized the LDA method developed in Fierro et al. (2012) and a three-dimensional variational (3DVAR) data assimilation (DA) technique-based radar DA, respectively, Fierro et al. (2014) demonstrated that assimilating lightning data could achieve similar improvements for the short-term forecast of this type of convective system as assimilating radar data. Fierro, Clark, et al. (2015) described the improvements when applying their LDA method on the precipitation forecast during the warm season of the United States. Lynn et al. (2015) and Lynn (2017) made use of the LDA scheme in Fierro et al. (2012) to evaluate its impact on lightning forecast and also tested a method to suppress spurious precipitation. Marchand and Fuelberg (2014) employed the low-level warming nudging method to initialize convection indicated by observed lightning at the convection-allowing scales. Qie et al. (2014) implemented a hyperbolic tangent-nudging function, which was similar to that in Fierro et al. (2012), into the Weather Research and Forecasting's (WRF) single-moment 6-class bulk microphysics scheme (Hong & Lim, 2006) to adjust the graupel mixing ratio (q_g) based on total lightning rate; however, the thermodynamic variables were not adjusted in their method.

Besides the nudging-based assimilation methods, several researchers employed ensemble Kalman filter (EnKF) and 3DVAR techniques to assimilate lightning data. Mansell (2014) employed an explicit lightning scheme and a linear relationship between flash rate and graupel echo volume, respectively, as forward operators to assimilate flash-extent density (FED) data with EnKF. Allen et al. (2016) tested model-based linear-forward operators between FED and graupel mass, graupel volume, and noninductive charging rate, respectively, with EnKF. They found that the operators of noninductive charging rate performed poorly compared to the operators of graupel mass and graupel volume. Fierro et al. (2016) utilized FED data and lightning source density data to calculate the pseudo-observations of the water-vapor mixing ratio and then assimilated them into the model in tandem with the radar data based cloud analysis algorithm within a 3DVAR framework. They also assimilated radial winds variationally using the full cost function with both $R < 10$ km and $R > 10$ km decorrelation length scales. They suggested multiscale approach for assimilating radar and lightning in future research endeavors.

This study presents a LDA nudging method implemented in the NCAR (National Center for Atmospheric Research) WRF Real-Time Four-Dimensional Data Assimilation (WRF-RTFDDA) system. In this LDA method, q_g fields are retrieved from the observed total lightning rates, then the retrieved q_g fields and the corresponding latent heat releases are assimilated into the WRF model via the nudging-based four-dimensional data assimilation (FDDA) method. The latent heat release is presented as the temperature tendency term in the model. Adjustment of latent heat associated with the added hydrometeor is important for promoting and sustaining convection, as well as making the model thermodynamic fields consistent with the lightning retrieved q_g fields. The LDA method proposed in this work is conceptually similar to that developed by Fierro et al. (2012), which directly promotes convection at observed lightning locations. In this LDA method, the lightning-retrieved q_g fields are assimilated simultaneously along with the latent heat releases into the WRF model based on the well documented, robust relationship between lightning rates and graupel contents. The main idea for this LDA method was also motivated by techniques used in modern cloud analysis packages (Gao & Stensrud, 2012; Hu et al., 2006; Xue et al., 2003).

2. Data and Methodology

2.1. Data

The data assimilated into WRF-RTFDDA for this work are the total lightning (i.e., a sum of cloud-ground (CG) and intracloud (IC) lightning) rate data from the ENTLN (Liu & Heckman, 2010). The detection efficiency of the ENTLN is more than 95% for CG flash and generally 50% to 90% for IC flash. The accuracy of detection location of the ENTLN is from tens of meters to about 500 m (see Figure 6 in Fierro et al., 2012). The total lightning data were interpolated to model grids (3 km × 3 km) from the original longitude and latitude coordinates and accumulated at intervals of 15 min (similar to the procedures in Fierro et al., 2012).

The data for model performance evaluation include the National Mosaic and Multisensor Quantitative Precipitation Estimation (NMQ) radar reflectivity product (Zhang et al., 2011), the NCEP's STAGE-IV precipitation data (Lin & Mitchell, 2005), the 2 m temperature and relative humidity data from the land-based weather stations, and the lightning data. The STAGE-IV precipitation data and the NMQ reflectivity data were interpolated to the model grid (3 km × 3 km) to establish direct comparisons with the simulations.

2.2. NCAR WRF-RTFDDA System

WRF-RTFDDA is a four-dimensional DA and forecasting system developed by NCAR. The RTFDDA system was originally built upon the Fifth-Generation Pennsylvania State University-National Center for Atmospheric Research Mesoscale Model (Grell, Dudhia, & Stauffer, 1994) and was later improved and incorporated into the WRF model by Liu et al. (2005, 2006). RTFDDA is formulated to continuously assimilate diverse weather data, including the rawinsonde, metar, ship, buoy reports, wind profilers, satellite atmospheric motion vectors, commercial airline reports, and radar, into the WRF model by a nudging/Newtonian relaxation approach. During the DA periods, it calculates the differences between the observation and model states, and then nudges the model state toward the observation by adding a tendency term to the model prognostic equations with temporal and spatial weight functions (Cheng et al., 2017; Liu, Warner, Astling et al., 2008; Liu, Warner, Bowers et al., 2008; Pan et al., 2015; Sharman et al., 2008).

There are two FDDA methods used in WRF-RTFDDA (Liu et al., 2006; Stauffer & Seaman, 1990): the observation nudging and the grid nudging. In the grid nudging, model states are nudged toward the observations at corresponding analysis-model grids, as expressed by equation (1):

$$\frac{\partial X_g}{\partial t} = P(X_g, t) + G_X \cdot W_X \cdot T_X \cdot (Y_g - X_g) \tag{1}$$

where X_g is the model-state variable, $P(X_g, t)$ is the original dynamical and physical terms of the WRF model prognostic equations, G_X is the relaxation time scale that is used to prevent the occurrence of unrealistic noise wave due to the instantaneous change of model variable, W_X is a spatial weight function, T_X is a time weight which is a function of the time lags between the observation and model state, and Y_g is the observation or analysis value on the model grids.

2.3. Lightning Assimilation Scheme

Based on the robust relationship between total lightning rate and graupel content/volume (e.g., Carey et al., 2014; Deierling et al., 2008; Fierro et al., 2006; Wiens et al., 2005), we retrieved q_g fields using the observed lightning rates and then assimilated them into the WRF model using the RTFDDA grid-nudging module along with latent heat nudging. As with the retrieval of hydrometeor mixing ratio from radar reflectivity in radar DA, some empirical assumptions are required to retrieve q_g fields from the total lightning rates.

The linear formulation between lightning rate and graupel mass (equation (2)) was derived in Alabama during the Deep Convective Clouds and Chemistry field experiment by Carey et al. (2014) using dual-polarimetric radar and lightning mapping array observations:

$$F = 2.43 \times 10^{-8} \cdot M_g \tag{2}$$

where F is the total lightning rate (per min) and M_g is the integral graupel mass (kg) in the layer confined between the $-10°C$ and $-40°C$ isotherms. In contrast to the relationship between rainfall and lightning, which is highly regime-dependent (e.g., Petersen & Rutledge, 1998), researchers found that the relationship between graupel mass and total lightning rate is relatively invariant for different regions and independent of meteorological regime (e.g., Deierling et al., 2008; Petersen et al., 2005). Therefore, although equation (2) was
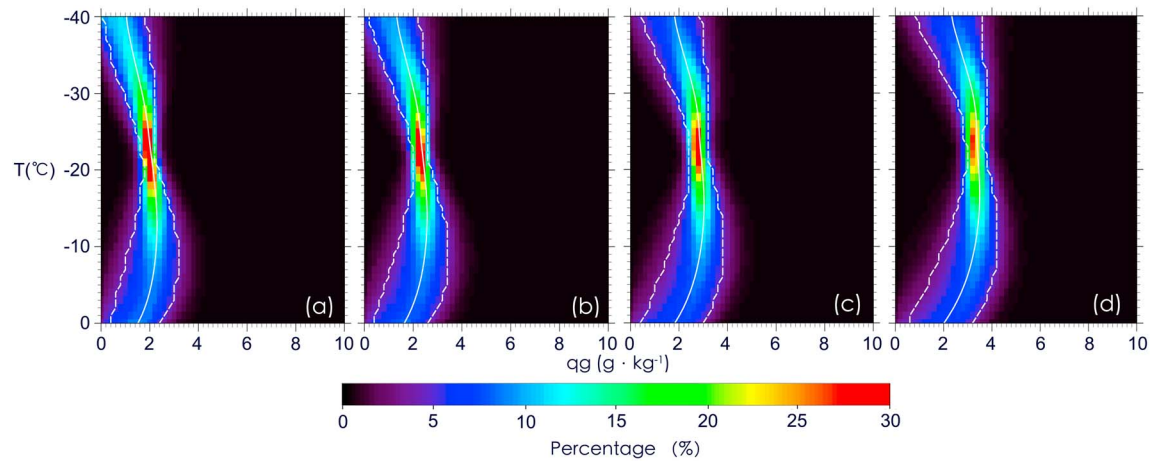
Figure 1. The frequency distribution diagrams of q_g corresponding to temperature for the (a) first, (b) third, (c) fifth, and (d) seventh bins of column-integrated graupel mass. The white lines are the characteristic profiles of q_g of the given bin, and the adjacent white dash lines are the 10th and 90th percentiles. The samples for the statistical profiles of these four bins are 28,075, 42,395, 27,462, and 17,796, respectively.

derived from the observation in Alabama, it could be applicable to other areas. It is noted that equation (2) was constructed on the whole-storm scale. Allen et al. (2016) found that graupel mass is well correlated with FED on the whole-storm scale and the subsections of storms on the scale of 8 km × 8 km. Gauthier et al. (2006) reported a near linear relationship between CG lightning rates and integrated precipitation ice mass on the column scale (2 km × 2 km) by analyzing 7 years of radar data and lightning data. Hence, we made an assumption that the linear equation between F and M_g on the whole-storm scale could be applied to the model-column scale.

The column-integrated graupel mass (between −10°C and −40°C) was calculated from the observed total lightning rates using equation (2). Since the column-integrated graupel mass is primarily determined by the q_g of each grid within the model-column, an approach to derive the three-dimensional q_g fields from the column-integrated graupel mass is to apply the characteristic profiles of q_g for different column-integrated graupel masses. A database of q_g profiles was constructed based on the retrospective simulation results of all severe convective weather cases during the 4 months from April to July of 2015 in central United States. The model physical schemes used in the retrospective simulations were the same as those used in the assimilation simulations, which will be introduced below. The retrospective simulations were run with a configuration of convection-allowing scale (3 km × 3 km) and dense model vertical levels in the layer between the 0°C and −40°C isotherms. The grid spacing of the retrospective simulations used to derive the database of q_g profiles needs to be the same as for the simulation domain used in the LDA experiments, as the characteristic profile of q_g for each bin of column-integrated graupel mass may likely be dependent on the grid spacing of the simulations. The outputs of the retrospective simulation were sampled every hour to construct the database of q_g profiles. Since the vertical distribution of q_g is more related to temperature than to altitude, when constructing the database of q_g profiles, each q_g sample profile was linearly interpolated to temperature layers in 1°C increments from the WRF model sigma levels. From the statistical results, the q_g within the 0°C to −10°C layer were found to be related to the integrated graupel mass between −10°C and −40°C (Pearson's $r > 0.80$), and the correlations were statistical significance ($p \leq 0.05$). Therefore, the q_g profiles with the temperature range between 0°C and −40°C were constructed. For each q_g profile, the corresponding column-integrated graupel mass (between −10°C and −40°C) was computed. In the database, the q_g profiles were divided into 13 groups according to the different column-integrated graupel mass bins. The characteristic profile of q_g for each bin of column-integrated graupel mass was determined by averaging the individual model-derived profiles that fell within the same group. The frequency distribution diagrams of q_g were constructed for each column-integrated graupel mass bin. Four examples of these diagrams are presented in Figure 1. The characteristic profiles of q_g and a series of percentiles are also shown in Figure 1.

In the ENTLN, for each lightning event, only the location of the brightest pulse (i.e., around the initiation location for IC lightning; the return-stroke location, which is usually not horizontally far away from the initiation location, for CG lightning) is recorded as the lightning location (M. Stock, personal communication, 2016).

Studies found that most lightning is initiated within or close to the regions containing graupel (e.g., Bruning et al., 2007; Fierro, Mansell, et al., 2015; Lund et al., 2009). Therefore, it is expected that graupel exists not only in the observed lightning columns but also in the adjacent regions of these columns. A distance-weighting function-based spread method was applied to account for the graupel in such regions (equations (3) and (4)):

$$q_g(x) = \frac{\sum_{i=1}^{N} q_g(x_i) \cdot W_i(r_i, R)}{N} \tag{3}$$

where q_g (x) is the q_g on grid-box x with zero lightning observation. q_g (x_i) is the q_g on grid-box x_i with nonzero lightning observation around grid-box x within the influence radius R. N is the number of grid boxes with nonzero lightning observations around grid-box x within the influence radius R. W_i is a spatial-weight function formulated by Cressman (1959) defined as

$$W_i(r_i, R) = \begin{cases} \dfrac{R^2 - r_i^2}{R^2 + r_i^2}, & 0 < r_i \leq R \\ 0, & r_i > R \end{cases} \tag{4}$$

where r_i is the horizontal distance between grid points x and x_i. The influence radius R was set to 6 km in this study. The areal extents of the retrieved q_g fields are linearly proportional to R. Several values of R were tested, and the value of 6 km appeared to produce the q_g fields that the areal extents were most consistent with the q_g fields retrieved from radar reflectivity data using the method of Lerach et al. (2010). Fierro et al. (2016) also used the decorrelation length scale of 6 km in their study. The total graupel mass of the whole domain is calculated before and after the spread process, respectively. After the spread process, the q_g on each grid box was decreased in equal proportion to keep the total graupel mass unchanged after the spread process. The q_g fields were then horizontally smoothed to mitigate sharp gradient. Figure 2 shows the examples of lightning-retrieved q_g fields (Figures 2a and 2c) and the corresponding lightning rates from observations (Figures 2b and 2d).

After the three-dimensional q_g fields were retrieved, they were assimilated into WRF using the RTFDDA grid-nudging module. The latent heat adjustment module of RTFDDA was employed to take into account the latent heat releases associated with the formation of the graupel. The temperature increments corresponding to the latent heat releases were proportional to the increments of q_g:

$$\Delta T = \Delta q_g [L_c(T_0) + L_f]/C_p \tag{5}$$

where ΔT is the temperature increments added to the tendency term, Δq_g is the increments of q_g of the grid box, L_c is the latent heat of condensation at the preexisting temperature T_0, L_f is the latent heat of freezing at 0°C, and C_p is the specific heat capacity of water. Below the 0°C layer and above the lifting condensation level, ΔT was linearly reduced from its value at the 0°C layer to zero. A filtering method for latent heat adjustments was applied, and the latent heat was added only at the grid where lightning-retrieved q_g was greater than 1 g kg^{-1} to prevent the excitation of strong updraft at the edge of convection. This filtering method is similar to that in Fierro et al. (2016), who set a lower cutoff value of lightning rate to avoid promoting the unrealistically wide updrafts. For the grid with zero lightning-retrieved q_g value, the background q_g, if it was greater than 0, was nudged toward 0 g kg^{-1}.

In this study, the LDA time interval is 15 min; for example, the lightning rate between 00:00:00 and 00:15:00 was assimilated into the model during the time integration between 00:00:00 and 00:15:00. Note that a thunderstorm may slightly move or evolve during one DA interval, while the lightning data are stationary during this period. The original time-dependent weighting function (T_x in equation (1)) of RTFDDA tends to mitigate such an effect. The time-dependent weighting function of the RTFDDA was modified for assimilating lightning data to account for the fact that lightning data are accumulated fields within a DA time window. This differs from radar DA where each recorded observation represents the information of a single moment, and therefore, the closer the model time is to the observation time, the higher the DA weight. In this LDA method, we set lower weights toward the boundaries of the two observation periods. For each LDA time window, in the first 2 min and last 2 min of each LDA time window, the weighting coefficient is set to zero; that is, the lightning is not assimilated, so that the simulated thunderstorms are freely adjusted by the model dynamics during these time segments. From the second minute to the third minute, the weighting function
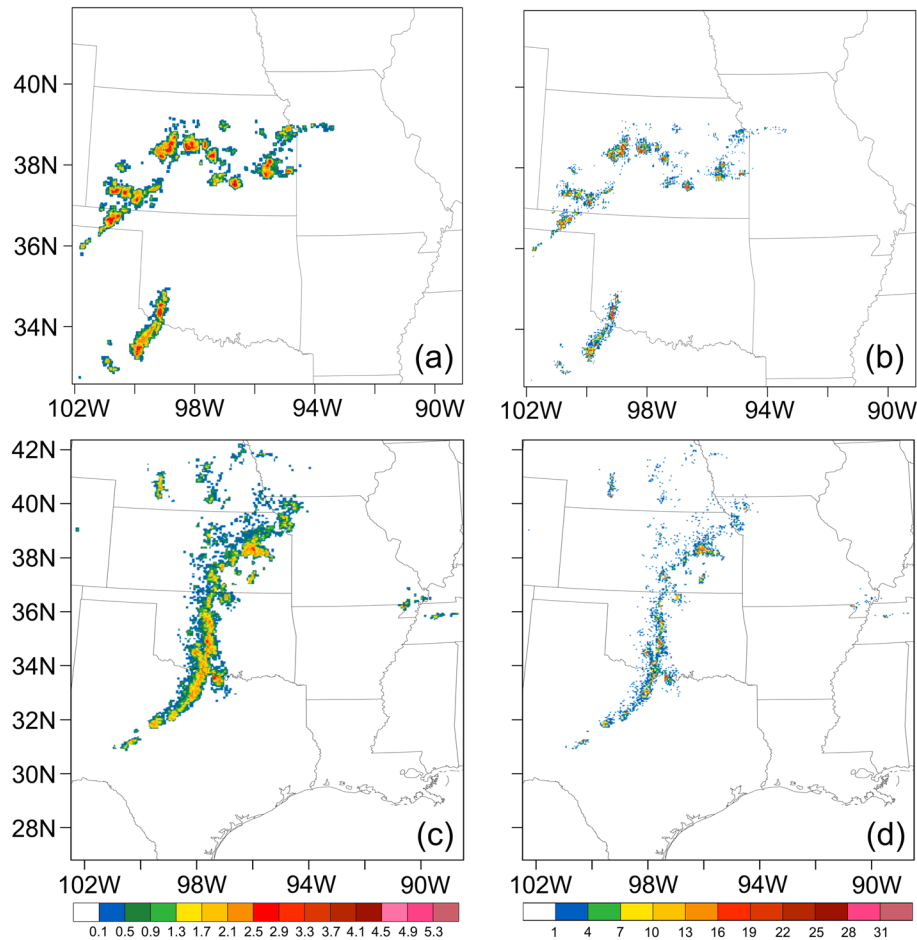
Figure 2. (a and c) q_g fields retrieved from the observed lightning rates (the maximum values in vertical; g kg^{-1}). (b and d) The corresponding total lightning rates from observations interpolated onto the WRF 3 km grid with 15 min accumulated interval.

gradually increases from 0.0 to 1.0, and the weighting function gradually decreases from 1.0 to 0.0 from the 12th minute to the 13th minute.

2.4. Case Descriptions and Model Configuration

Three convection cases with different characteristics, occurred in the central plains of the United States, were selected to test the LDA scheme.

Case 1. An organized squall line in the southern and central plains of the United States on 27 April 2016. The squall line was initiated around 2200 UTC 26 April over eastern Kansas, western Oklahoma, and northwestern Texas. It moved eastward into Missouri and Arkansas by 0600 UTC 27 April. The squall line was influenced by a deep low pressure (996 hPa) over Kansas, Oklahoma, and northwestern Texas.

Case 2. An MCS in the central plains of the United States on 3 July 2016, which grew upscale from several discrete storms over Colorado and Kansas. A surface low pressure (1,004 hPa) system was situated over Kansas, Oklahoma, and Texas.

Case 3. Outbreak of discrete storms in the central plains of the United States on 8 July 2017. With the development of the storms, some discrete storms gradually merged into an MCS. The outbreak of discrete storms was associated with strong local forcing.

The simulation domains for these three cases included one nested grid (Figure 3). The horizontal grid spacing was 9 km for the outer domain and 3 km for the inner domain. The lightning data were assimilated to the inner domain only. As the IC/CG flash ratio is generally around 3:1 in typical single or multicell thunderstorms (Boccippio et al., 2001), the average detection efficiencies for total lightning over the three simulation domains could be around 70%. Both domains had 43 vertical (WRF eta) levels and a model top at around
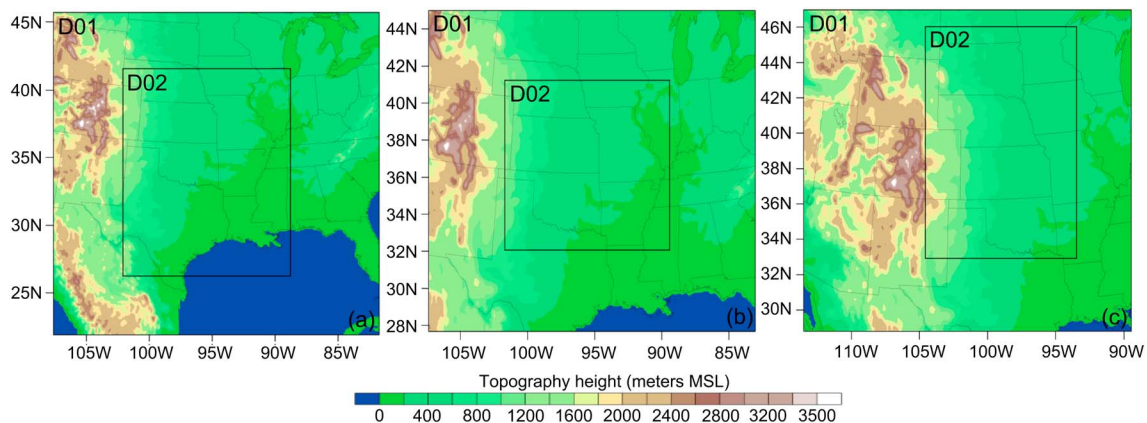
Figure 3. Model domain configurations for the case studies. (a) The case of 27 April 2016. (b) The case of 3 July 2016. (c) The case of 08 July 2017. Terrain heights are represented in colored shades.

50 hPa. The 6-hourly 0.25° NCEP Final Operational Global Analysis (FNL) data were used as initial and lateral boundary conditions. The NSSL-ELEC two-moment, six hydrometeor category bulk microphysics scheme (Mansell et al., 2010; Mansell, 2010; Ziegler, 1985) that is coupled with an electrification scheme (Mansell et al., 2005) and a bulk lightning discharge scheme (Fierro et al., 2013) was employed in this study. The NSSL-ELEC scheme is characterized by coupling electrification and lightning discharge scheme to WRF and enables WRF to simulate the charging processes and lightning of thunderstorms. The detailed descriptions of charging and lightning discharge schemes of NSSL-ELEC can be found in Mansell et al. (2005), Mansell et al. (2010), and Fierro et al. (2013). When using the NSSL-ELEC to explicitly forecast the flash origin density rates, the selected noninductive charging scheme was Saunders and Peck Scheme (Saunders & Peck, 1998; Mansell et al., 2005); the breakeven field profile (Dwyer et al., 2005) was used as the breakdown electric field profile to initiate lightning; the size of discharge cylinders was set to 6,000 m; the option of screening layers was switched off; the fraction of the electric field magnitude or net charge, which was removed within the cylinder volume after bulk discharge, was set to 0.5.

Other physical schemes employed in this study include the Mellor-Yamada-Janjic turbulence kinetic energy scheme for the boundary layer (Janjić, 1994), the Noah land surface model (Chen & Dudhia, 2001; Ek et al., 2003), and the Rapid Radiative Transfer Model for GCM shortwave and longwave radiation schemes (Iacono et al., 2008). The Grell-Freitas (Grell & Freitas, 2013) CPS was utilized in the outermost domain, while no CPS was activated in the 3 km inner domain.

Three sets of experiments were conducted with varying simulation and analysis time windows to evaluate the LDA. In the first set of experiments (Figure 4a), the simulations for all three cases were initialized at 0000 UTC and ended at 0900 UTC. In the experiments with the LDA, total lightning data were assimilated during the first 3 h (0000 UTC–0300 UTC) with a 15 min interval. In this set of experiments, there was no "spin up" period allowed prior to the LDA, and the model was "spun-up" dynamically along with the LDA process. In the second set of experiments (Figure 4b), a spin-up period occurred before starting the DA, and thus, the simulation results provided information on continuous DA cycles that mimic DA cycles of operational RTFDDA forecast systems. In the third set of experiments (Figure 4c), for all cases, the initial times are the same as the first set of experiments, but the time window lengths of the LDA were set to 2 h, 3 h, 4 h, and 5 h, respectively. One-hour and two-hour forecasts were performed after the LDA period. The last set of experiments was used to assess the effect of the LDA on nowcasting (0–2 h forecasts) of lightning and convective precipitation. For each case, a control experiment (without the LDA) was conducted. In the first set of experiments, the simulation using the LDA method developed by Fierro et al. (2012) was also performed for Case 1 for a comparison. The acronyms and description of all the experiments are summarized in Table 1.

3. Results

The model forecasts of radar composite reflectivity, total lightning densities, and surface precipitation with/without the LDA are evaluated through subjective comparisons and computing objective skill scores
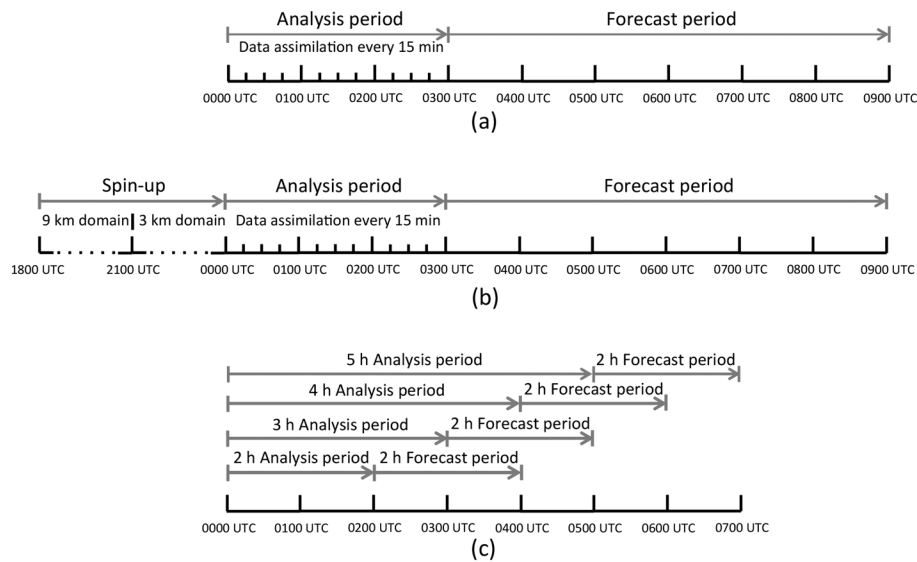
Figure 4. Flow diagrams for the experiments of (a) the LDA without a proceeding "spin-up" period, (b) the mimic cycled LDA system, and (c) employing the LDA on convection nowcasting.

against the corresponding observations. The simulation results of the first set of experiments were presented in section 3.1, section 3.2, and section 3.3.

3.1. Case 1: 27 April 2016

In ASML, the model q_g fields were continuously adjusted toward those retrieved from the lightning data and the corresponding latent heat releases were added through the thermodynamic equations during the analysis period. By 0300 UTC (i.e., the end of the analysis period), the overall morphology of the squall line of ASML matched well with the observation (Figures 5a–5c). ASML positioned the lightning and precipitation regions more accurately than CTRL did (Figures 6a–6c and 7a–7c). ASML well captured lightning activity and rainfall in north-central Texas, while CTRL failed to simulate those (black arrows in Figures 6b and 6c and 7b and 7c). These improvements were realized partly by the more accurate simulation of q_g fields in the analysis period (Figures 8a, 8b, 8e, and 8f), as graupel affects electrification and cold rain processes. In ASML, updrafts were promoted in the regions where the increments of q_g were added using the latent heat nudging (Figure 9b). Compared to CTRL, wider areal extent of updrafts in ASML (Figures 9a and 9b) caused a broad distribution of the water vapor. As a result, the areal extents of precipitation regions were increased and the maximum precipitation intensity was reduced, which were more consistent with the observations than those in CTRL (Figures 7a–7c).

During the analysis period, precipitation was generated faster in ASML compared to ASML-FO (not shown), as the graupel, which was directly assimilated into the model in ASML, could affect the cold-cloud precipitation microphysics (i.e., graupel melts into raindrops). The updrafts were promoted in both ASML and ASML-FO (not shown), while the cold pools were produced faster in ASML, as a result of the faster

Table 1
The Acronyms and Description of the First Set of Experiments (the First and the Second Row), the Second Set of Experiments (the Third Row), and the Third Set of Experiments (the Fourth Row)

| Experiment Names	If There Is a "Spin-Up" Before the Analysis Time	Forecast Time	Descriptions
CTRL, ASML	No	6 h	Control run and lightning data assimilation run (cf. Figure 4a)
ASML-FO	No	6 h	Lightning data assimilation run using the method developed by Fierro et al. (2012)
CTRL-SP, ASML-SP	Yes	6 h	Control run and lightning data assimilation run. Used to mimic DA cycles of operational RTFDDA forecast systems (cf. Figure 4b)
CTRL-NC, ASML-NC	No	2 h	Control run and lightning data assimilation run. Used to assess the effect of the LDA on nowcasting (0–2 h forecasts) of lightning and convective precipitation (cf. Figure 4c)
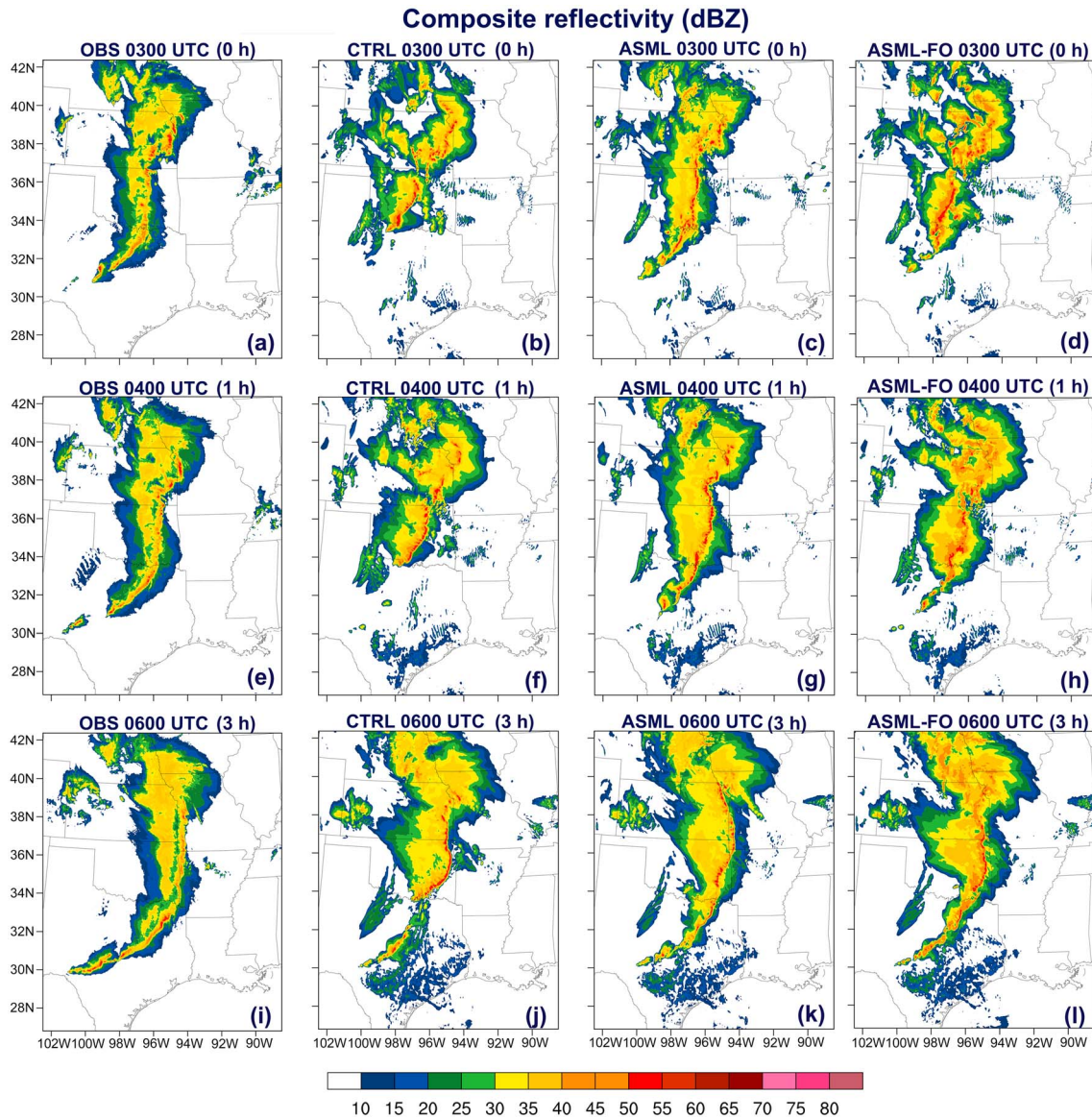
Figure 5. Composite radar reflectivity (dBZ) for the case of 27 April 2016. (a, e, and i) The NMQ observations; (b, f, and j) CTRL; (c, g, and k) ASML; (d, h, and l) ASML-FO. The time and valid forecast time (in the brackets) are marked above each panel; 0 h is the end of analysis period.

production of precipitation. The cold pool could affect the development of convection, and this effect is more pronounced on the cold pool-dominated storms (e.g., Case 1). The radar composite reflectivity of ASML was more consistent with the observations compared with ASML-FO during the analysis period (Figures 5a, 5c, and 5d). In ASML-FO, the coefficients used to increase water vapor (q_v) were the same as in Fierro et al. (2012) (i.e., the minimum relative humidity of 81% and the maximum relative humidity of 101%). An experiment with more aggressive q_v adjustments (similar to Fierro, Clark, et al., 2015; i.e., the minimum relative humidity of 95% and the maximum relative humidity of 105%) generated precipitation and cold pool slightly faster than using the coefficients in Fierro et al. (2012), but still slower than ASML did.

By 0400 UTC (1 h forecast), CTRL failed to forecast lightning and rainfall in north-central Texas (black arrows in Figures 6e and 6f and 7e and 7f), owing to a lack of graupel and updrafts at that area (Figure 8c). In contrast, in ASML, the q_g fields in northern Texas were maintained into the forecast period (Figure 8g), suggesting that the updrafts promoted by latent heat nudging were generally consistent with the assimilated q_g fields. In addition, ASML corrected the excessive lightning densities in Oklahoma of CTRL. Due to the faster
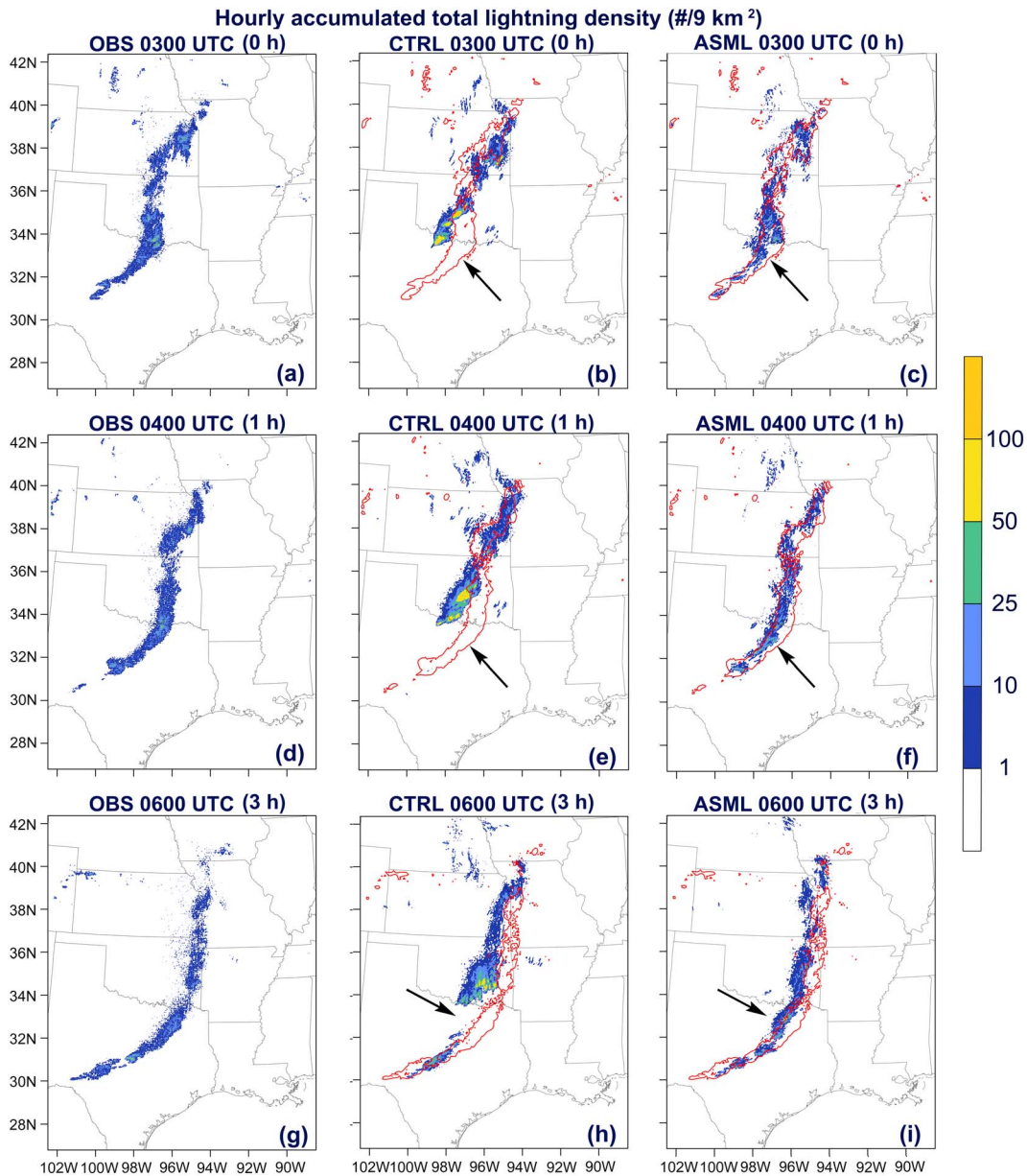
Figure 6. Hourly accumulated total lightning rates (at 9 km^2) up to the time marked in each panel (forecast time is shown in the bracket) for the case of 27 April 2016. (a, d, and g) The ENTLN observations; (b, e, and h) CTRL; (c, f, and i) ASML. The observation contour of 1 (at 9 km^2; in red) is shown in the panels of CTRL and ASML. The areas pointed by black arrows are specially discussed in the text.

production of cold pools in the analysis period of ASML, the morphology of the squall line of ASML was slightly better than that of ASML-FO in 1 h forecast (Figures 5e, 5g, and 5h).

By 0600 UTC (3 h forecast), CTRL forecasted some q_g fields in central Texas but failed to simulate q_g fields (Figure 8d) and updrafts (not shown) in northern Texas, resulting in lightning and rainfall gaps (black arrows in Figures 6h and 7h). The updrafts and q_g fields were maintained after the LDA period, and the continuous distribution of lightning and precipitation were forecasted in ASML (black arrows in Figures 6i and 7i), which agreed with the observations. The bias in propagation speed of the squall line in ASML was smaller than that in CTRL because of the existence of a deeper cold pool in ASML (Figures 9c–9f). At this time, the morphology of the squall line in ASML was very similar to that in ASML-FO (Figures 5k, and 5l).

The horizontal winds, relative humidity, and surface potential temperatures of the experiments were analyzed (Figure 9) to understand the role of the LDA in correcting the initial thermodynamic
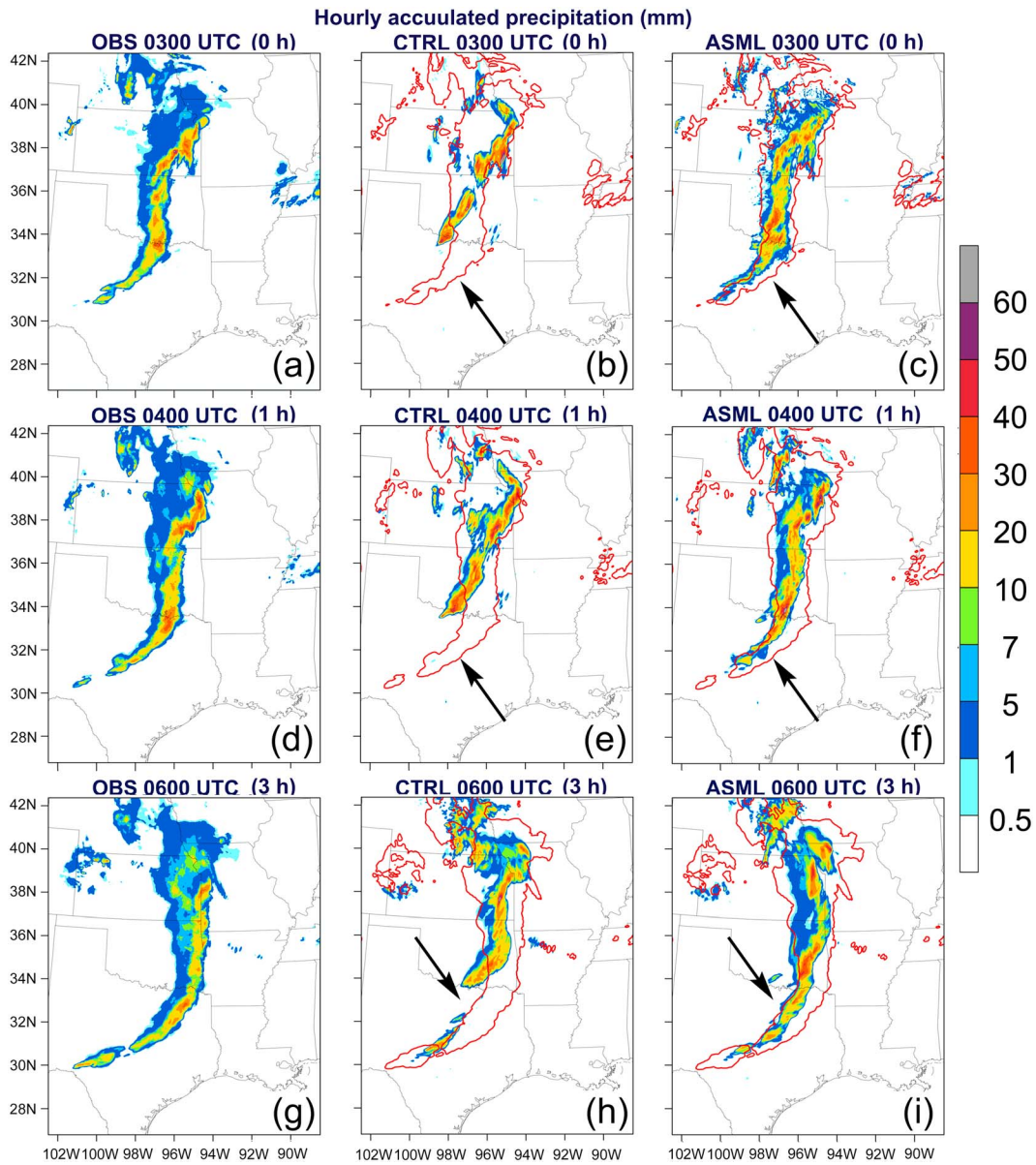
Figure 7. Hourly accumulated precipitation rates (mm) up to the time denoted above each panel (forecast time is shown in the bracket) for the case study of 27 April 2016. (a, d, and g) The STAGE-IV observations; (b, e, and h) CTRL; (c, f, and i) ASML. The observation contours of 0.5 mm (in red) are shown in the panels of CTRL and ASML. The areas pointed by the black arrows are discussed more specifically in the text.

environment. In CTRL (Figure 9c), although the convergence existed across the dry line, the thermodynamic environment in north-central Texas with warmer air on the west side of the dry line and colder on the east side was not favorable for the initiation of convection. Figure 9e shows that the simulated temperature of CTRL was more than 6°C higher than the observation in the south part of the convergence (indicated by the lower violet frame in Figure 9e), indicating that the areal extent of the north-south-oriented cold front in CTRL was smaller than the observation. The biases of temperature fields and the associated cold front are the main reasons for CTRL to fail in simulating convection in Texas in CTRL. The positional deviation of the cold front resulted in the forecasted squall line to be displaced from the observations. In contrast, the convection in Texas was triggered by the LDA during the analysis period of ASML (Figure 9b), and the associated rainfall produced cold pools in Kansas, Oklahoma, and Texas (Figure 9d). The LDA-introduced cold pools reduced the local simulation errors in temperature (Figure 9f, indicated by the violet frames). The eastward movement of the cold pools continuously lifted the warm moist air masses on the east side of the fronts and maintained convections during the subsequent forecast period (not shown). The
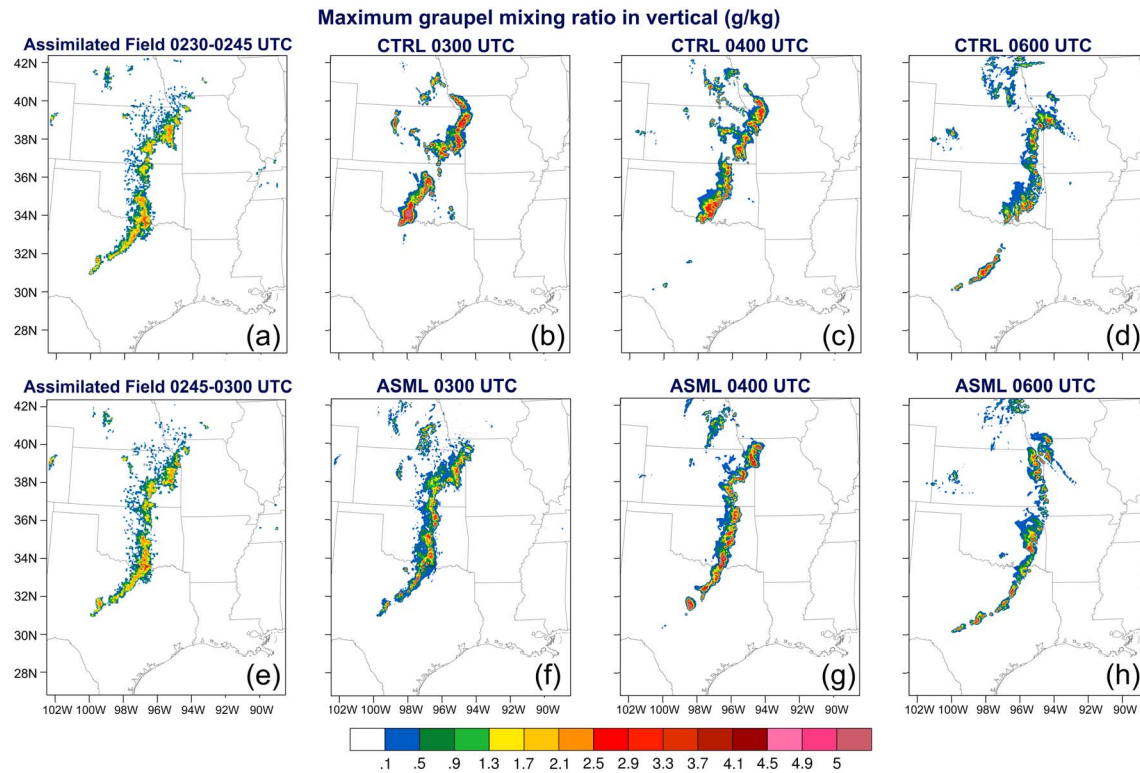
Figure 8. For the case study of 27 April 2016. (a and e) The lightning retrieved q_g fields (g kg^{-1}; the maximum values in vertical) that are assimilated into the model during the time marked in each panel. The simulated q_g fields (g kg^{-1}; the maximum values in vertical) of (b–d) CTRL and (f–h) ASML.

corrected convection in ASML improved the simulation of the cold front locations and resulted in better forecasts of the squall line locations during the forecast period.

3.2. Case 2: 3 July 2016

At 0300 UTC (i.e., the analysis period), ASML noticeably improved the lightning (Figures 10a–10c) and precipitation (Figures 11a–11c) simulations compared to CTRL, which benefited from the assimilation of the lightning-retrieved q_g fields and the promotion of updrafts. The widespread stratiform precipitation of the observed MCS was simulated in ASML, but there were only smaller and isolated precipitation regions in CTRL (Figures 11a–11c). The stratiform region of the storm was found to influence the local dynamic and thermodynamic environments of the MCS (Houze, 2004; Peters & Schumacher, 2014) and therefore affected the subsequent development of the MCS. ASML appeared to "spin-up" the convection quickly. The convection was produced during the first hour of the analysis period, while no convection was developed in CTRL at the same time (not shown).

By 0400 and 0600 UTC (1 h and 3 h forecasts, respectively), ASML predicted the locations and areal extents of lightning (Figures 10d–10i) and rainfall (Figures 11d–11i) regions more accurately than CTRL did. The forecast lightning and rainfall regions in CTRL showed a westward deviation from the observations. However, the lightning densities in ASML were smaller than observed, especially in northwestern Oklahoma (black arrows in Figures 10f and 10i). The q_g there was marginal owing to weakening updrafts (not shown); therefore, lightning was sparse.

To explain the forecast improvements seen in ASML, the horizontal wind field relative humidity and surface temperatures were analyzed. In CTRL, the dry environment in southwestern Kansas (the near-surface relative humidity was 30–40% drier than the observation) and the weak temperature gradients in central Kansas were not favorable for the generation of strong convection. Therefore, updrafts were weak (not shown). In ASML, the convections were forced at the observed lightning locations during the analysis time. The heavier rainfall resulted in increased evaporative cooling, thereby producing cold pools in Kansas, Oklahoma, and Texas stronger than those in CTRL. The associated southeastward spread outflow boundary led to stronger
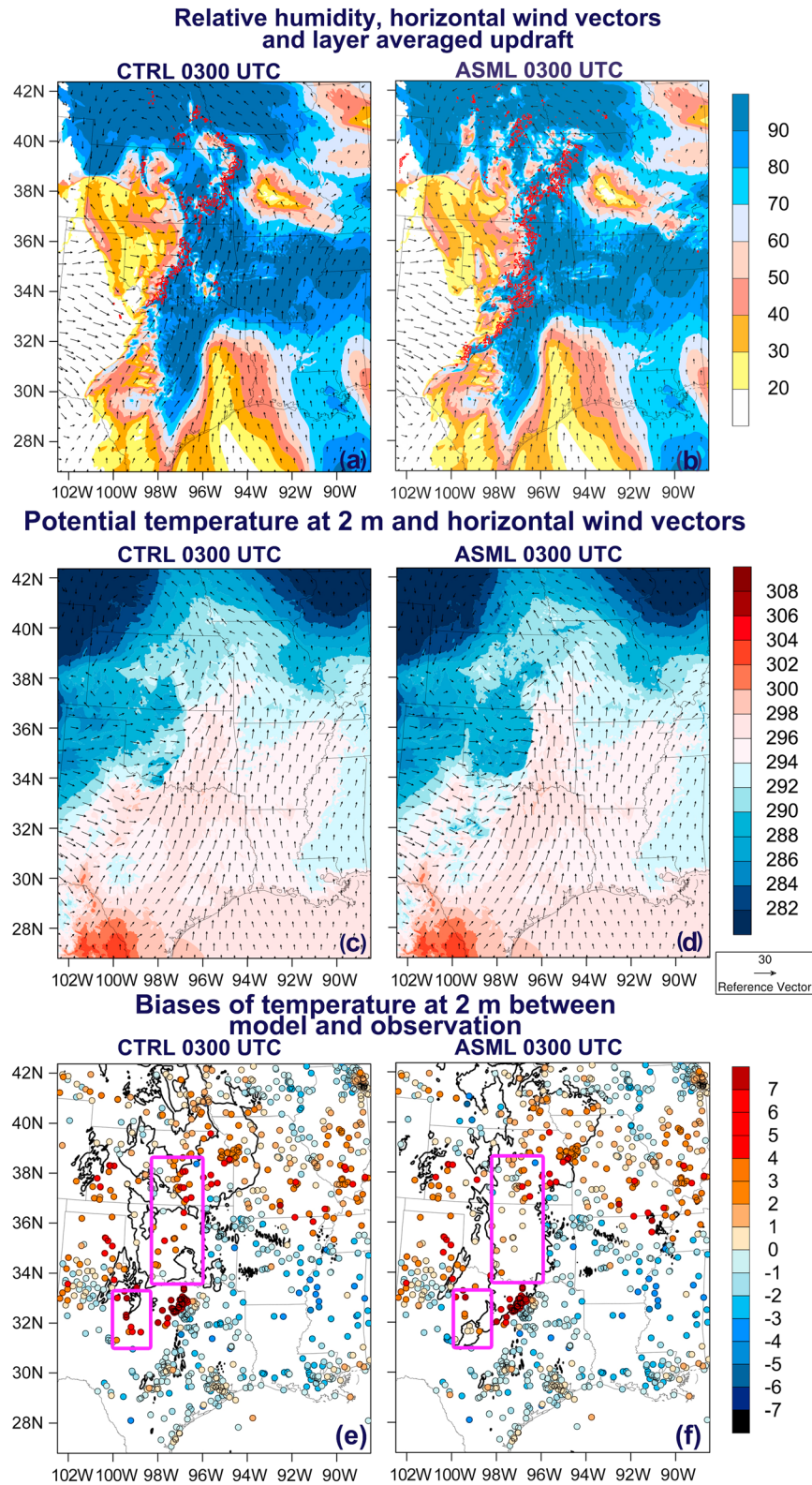
Figure 9. The averaged vertical velocities between 3 km to 10 km MSL (red contours; contour of 2 m/s) and the 850 hPa relative humidity (shading; %) for (a) CTRL and (b) ASML. The 2 m potential temperature (shading; K) overlaid with the 850 hPa horizontal wind fields (wind arrows; m s^{-1}) for (c) CTRL and (d) ASML. The biases of the simulated 2 m temperature (colored circles; °C) for (e) CTRL and (f) ASML. The observed temperatures are from ground meteorological stations. The 20 dBZ radar composite reflectivity contours (in black) are shown. The areas inside the violet frames highlight the reduced biases in ASML and are discussed in the text. The valid time is shown above each figure.
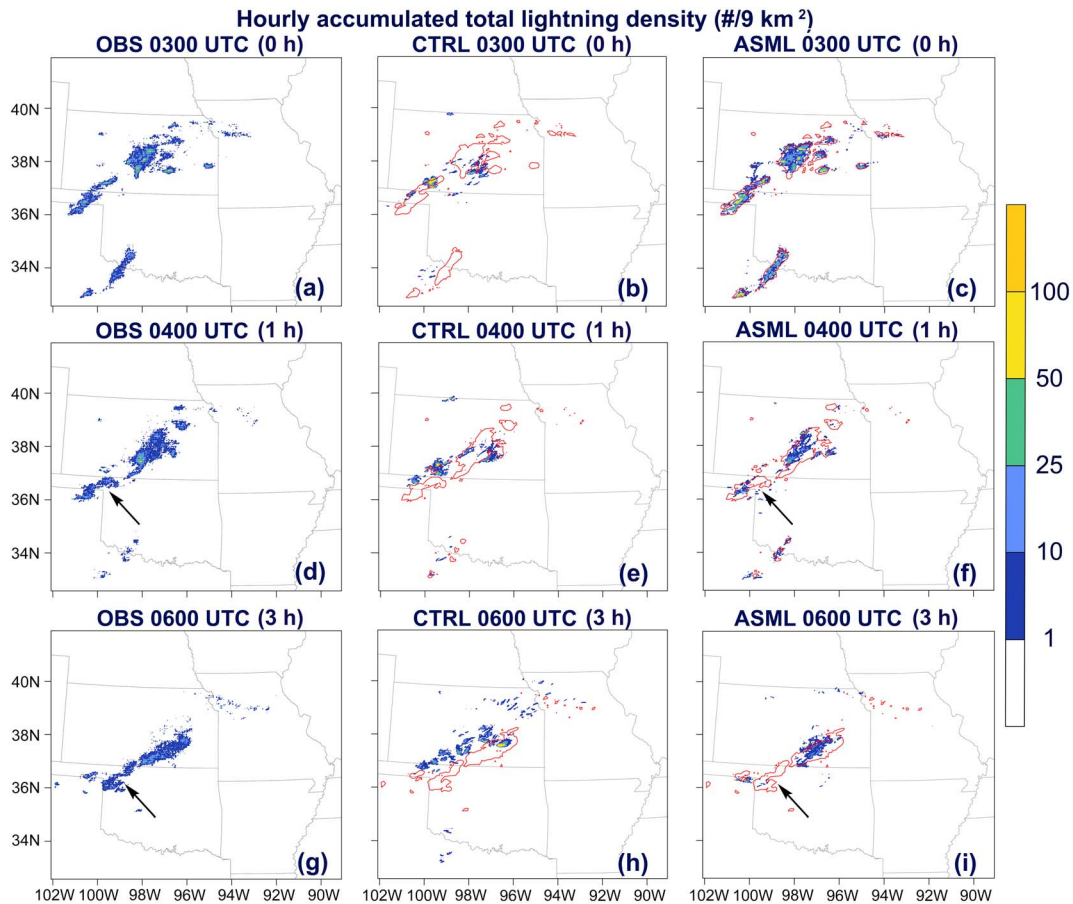
Figure 10. As in Figure 6, but for the case study of 3 July 2016.

convergences along the convective lines than those in CTRL (not shown). The air in central Kansas was moist (not shown) and provided water vapor to support the development of the northeast part of the MCS during the forecast periods. However, the air in northwestern Oklahoma, which was ahead of the outflow boundary of the southwest part of the MSC, was dry (the near-surface relative humidity was 30% drier than the observation; not shown). The southeastward advancing outflow boundary was not able to trigger the strong secondary convection along the outflow boundary because the dry environment was unfavorable for strong kinematic lifting. In the region ahead of the MCS, the relative humidity biases could not be corrected by the storm-scale LDA (not shown). Thus, large-scale background biases may limit the effect of LDA.

3.3. Case 3: 8 July 2017

At the end of the analysis period (i.e., 0300 UTC), the discrete storms were simulated in ASML, and an MCS, which resulted from the merger of two discrete storms, was well reproduced (Figure 12c). At this time, CTRL failed to simulate most of the discrete storms (Figure 12b). During the analysis period, the locations of lightning and precipitation regions were overall consistent with the observations in ASML, although there were quantitative biases (not shown). In the forecast period, although ASML improved the forecasts compared to CTRL, the consistency between the simulations results of ASML and observations worsened. Some discrete storms were not maintained in the forecast period (black arrows in Figure 12f), and the updrafts at those locations weakened shortly after the LDA period (not shown). Despite the increase in latent heating at those locations, the lack of convergence did not allow those storms to persist.

By analyzing the wind fields and surface temperature fields of ASML, we found that there was no convergence in the locations of the storms that decayed shortly after the LDA period (not shown). The initial and boundary conditions derived from the 0.25° FNL data might not well capture such small-scale local
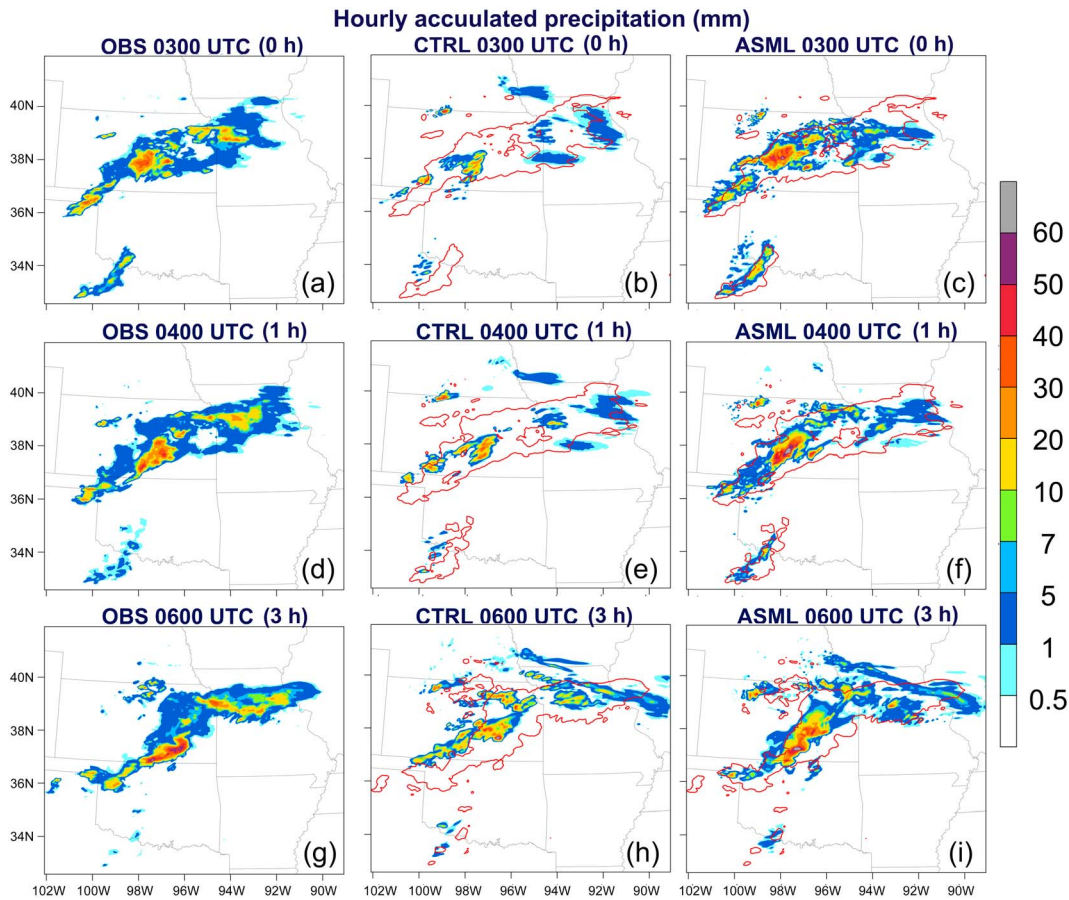
Figure 11. As in Figure 7, but for the case study of 3 July 2016.

convergences. The promoted updrafts could not be maintained in such environment, which was unfavorable for the development of individual storm. As indicated by Fierro et al. (2015), the forecast of the individual severe storm depends, among other factors, on a balance between wind shear, cold pool strength/size, and thermal instability, which is more difficult to achieve than in the case of well organized MCSs. Therefore, the forecast for the individual severe storm will be more sensitive to the background errors in the initial and boundary conditions.

3.4. Quantitative Evaluation of Lightning and Precipitation Forecasts

To evaluate the forecast results quantitatively, fraction skill scores (FSSs) (Roberts & Lean, 2008) were calculated for lightning and precipitation forecasts of the three sets of experiments. The advantage of FSS is that it provides a reliable assessment of displacement errors. In addition, it can be more tolerant to small displacement errors compared with the ETS (equitable threat score), which makes it more suitable for the evaluation of the simulation with fine scale grids. The ENTLN total lightning data and the STAGE-IV precipitation data were used as references. FSSs for different neighborhood radii from 3 to 45 km (i.e., 1–15 neighborhood grid points) and different thresholds were calculated, and the results for the 24 km neighborhood radius at the thresholds of $1/9$ km^2 (for lightning forecasts) and 5 mm (for precipitation forecasts) were presented herein. For the first (cf. Table 1) and the second (cf. Table 1) sets of experiments, the 0–6 h short-term forecasts were evaluated. For the third set of experiments (cf. Table 1), the nowcasting (0–2 h) results were evaluated.

The variation characteristics of the FSSs over the forecasts for hourly-accumulated lightning (Figures 13a–13c) were similar to those for hourly-accumulated precipitation forecasts (Figures 13d–13f). The experiments with the LDA all produced higher FSS than the experiments without the LDA. As the forecast time progressed, the FSSs of ASML gradually dropped. The differences in FSS between ASML and CTRL lessened. The FSS
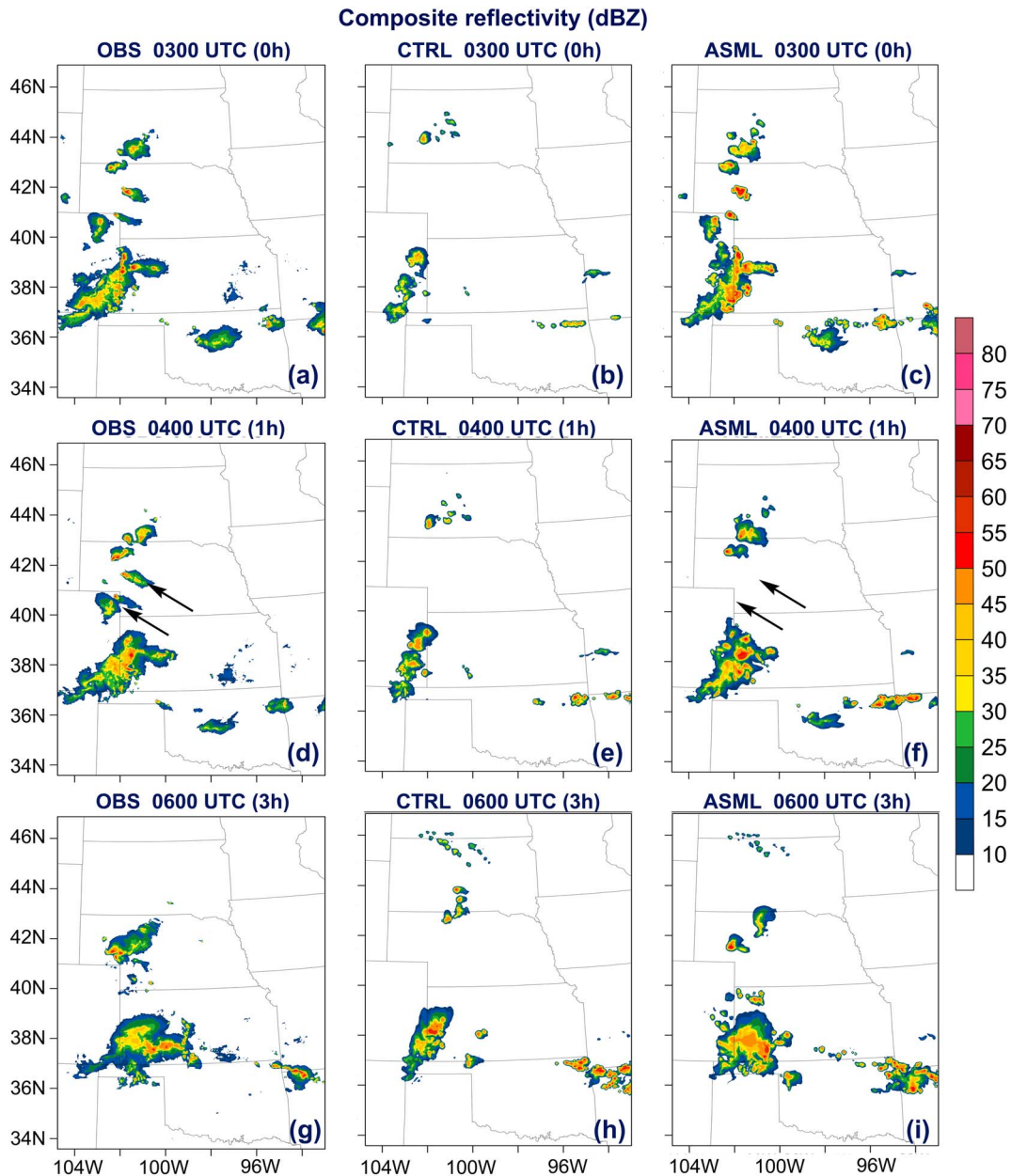
Figure 12. As in Figure 5, but for the case study of 8 July 2017. The areas pointed by the black arrows are discussed more specifically in the text.

results of the experiments with a "spin-up" time before the analysis time showed negligible differences from those without a "spin-up" time (not shown). The statistical significance tests were performed for the differences in FSS between ASML and CTRL using paired t test. The statistical significance test results showed that the differences in FSSs between ASML and CTRL at all selected thresholds and neighborhood radii were statistically significant at 95% confidence level. For Case 1, ASML performed better than ASML-FO in the first 4 h of the forecast time, which could be due to the faster production of the cold pools (Figure 13a). ASML-FO performed better in the 5 h and 6 h forecasts.

The variation characteristics of the FSS over forecast time were similar to those reported in Fierro, Clark, et al. (2015) (precipitation forecast) and Lynn et al. (2015) (lightning forecast), who used a relative humidity adjustment based storm-scale LDA method developed by Fierro et al. (2012). The main reason for such variation characteristics was that model solution was gradually saturated by the errors within the initial/boundary conditions provided by FNL (as indicated by Fierro, Clark, et al., 2015). Additionally, the LDA mostly corrected the
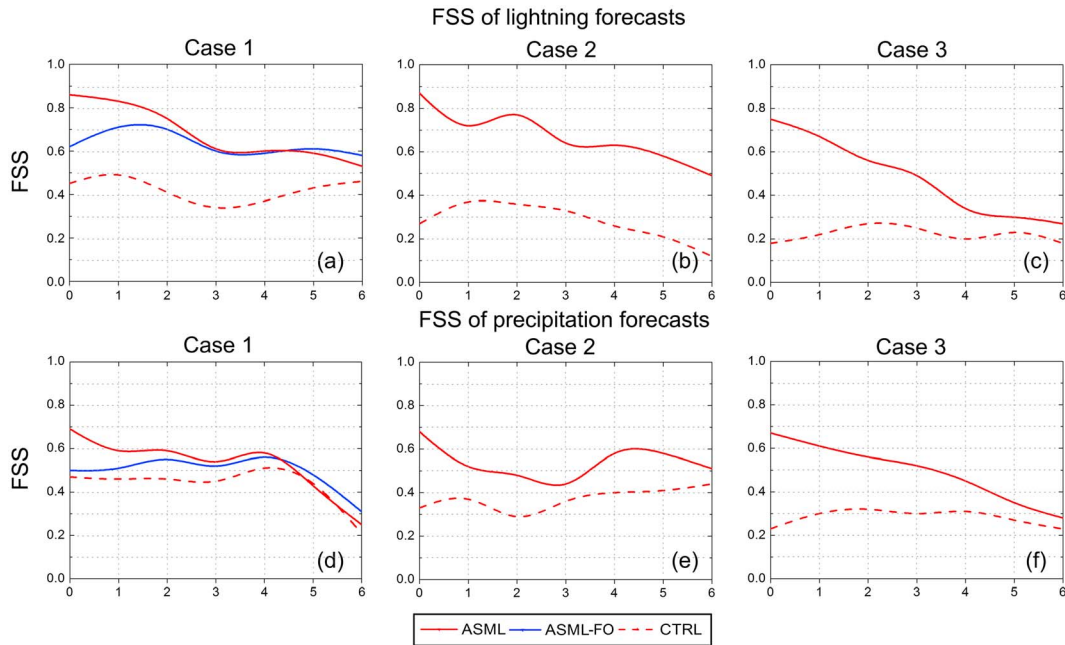
Figure 13. FSS of the hourly-accumulated (a–c) lightning and (d–f) precipitation forecasts. The case numbers are shown on the top of each panel. For case 1, one assimilation experiment was performed using the LDA method developed by Fierro et al. The neighborhood radii are 24 km, and the thresholds for lightning forecasts and precipitation forecasts are 1 (at 9 km^2) and 5 mm, respectively. 0 h represents the end of the analysis period.

storm-scale model states and had minimal effect on the large-scale environments. At the early stage of the forecast, the storm-scale features played a major role. As time progressed, the role of the large-scale environment became more influential (Johnson et al., 2015).

To focus on the impact of the LDA on convection nowcasting, we evaluated a series of the lightning and precipitation nowcasting (0–2 h forecasts) results (cf. Table 1). The FSSs of the lightning and precipitation
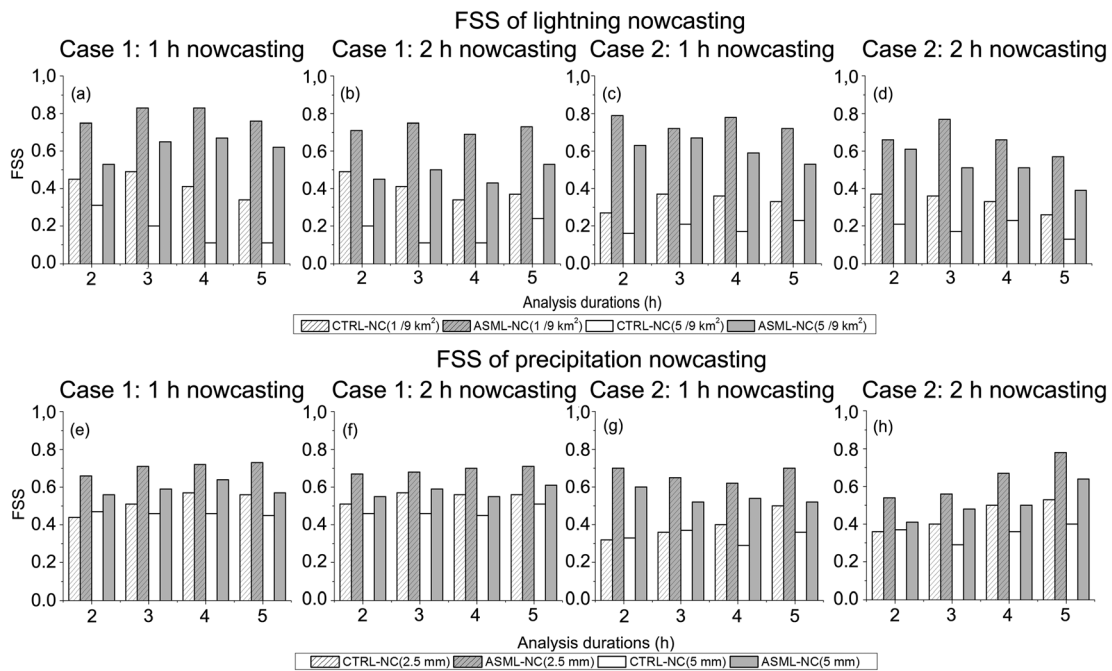

Figure 14. FSS of the hourly accumulated (a–d) lightning and (e–h) precipitation nowcasting (1 h; 2 h forecasts). The experiments with 2 h, 3 h, 4 h, and 5 h analysis durations are performed. In each experiment, CTRL-NC and ASML-NC have the same analysis duration. The neighborhood radii for all panels are 24 km. The case numbers are shown on the top of each panel. The thresholds are shown in the figure legends.

nowcasting of Case 1 and Case 2 are shown herein (Figure 14). It was found that the LDA noticeably improved the accuracy of lightning nowcasting (Figures 14a–14d). The lightning nowcasting FSSs of CTRL-NC hardly exceeded 0.5 for the threshold of 1 (at 9 km^2) and 0.3 for the threshold of 5 (at 9 km^2), while ASML-NC increased the FSSs by 0.2–0.5. This result demonstrated that the LDA could be an effective way to improve lightning nowcasting that is highly desirable by many applications. The LDA also significantly improved convective scale precipitation nowcasting (Figures 14e–14h). Although the improvements were not as outstanding as the improvements in the lightning nowcasting, ASML-NC improved precipitation FSSs by 0.1–0.3 in most cases.

4. Discussion and Conclusions

An LDA method implemented in the NCAR WRF-RTFDDA system was developed wherein q_g was used as the proxy of total lightning rates. In this LDA method, column-integrated graupel mass is first calculated using an observation-based linear formula between graupel mass and observed lightning rates. Then three-dimensional q_g fields are retrieved from column-integrated graupel mass by constructing and employing simulated characteristic profiles of q_g for different integrated graupel mass bins and utilizing a horizontal Cressman spread process. A horizontal spread algorithm for q_g is used to account for the existence of graupel in the adjacent regions of lightning initiation points. The latent heat releases corresponding to the formation of the retrieved graupel are then computed. The retrieved q_g fields and corresponding latent heat increments are nudged into the WRF thermodynamic and microphysical equations with the latent heat and hydrometeor adjustment module of the RTFDDA system.

Three high impact weather cases were simulated to evaluate the impact of the LDA scheme on the short-term (0–6 h) lightning and precipitation forecasts. Both of subjective comparisons and qualitative evaluations were performed against the observations. The results showed that the experiments with the LDA outperformed the control experiments for 0–6 h lightning and precipitation forecasts and the LDA improved the analysis and forecasts of q_g fields, updrafts, cold pool, and front locations.

Currently, the main methods for operational nowcasting of severe convection weather are essentially based on variant forward extrapolation methods. The extrapolation techniques usually outperform the more complex NWP in 0–2 h lead times (e.g., Sun et al., 2014). In this study, we demonstrated that LDA is an effective approach for producing lightning and convective weather precipitation nowcasting (0–2 h ahead).

In Cases 2 and 3, the errors in humidity, temperature, and wind fields existing in the large scale background negatively affected the effects of the LDA, and some promoted convection cells in the analysis time were not well maintained in the forecast time. Further studies will test the effect of the multiscale DA, which combines the storm-scale LDA with the synoptic and mesoscale conventional observations DA on the accuracy of lightning and precipitation forecasts. Similar to the results in Fierro, Clark, et al. (2015), who used a relative humidity adjustment based storm-scale LDA method, the present LDA method also performed less well on the forecast of the individual severe convective cell compared with the outflow-dominated MCS. As noted by Fierro, Clark, et al. (2015), the forecast of the outflow-dominated MCS mainly depends on the simulation of the location and strength of cool pool, while the forecast of the individual severe storm heavily depends, among other factors, on a balance between wind shear, cold pool strength/size, and thermal instability, which is more difficult to achieve than in the case of well-organized MCSs. Therefore, forecast for discrete storms is more sensitive to the background errors.

Compared to the LDA methods using pseudo-q_v or temperature increments to promote convection, assimilating q_g retrievals along with the latent heat could reproduce the q_g fields, precipitation, and cold-pool faster. Nevertheless, uncertainties exist in the process of retrieving the three-dimensional q_g fields by using total lightning rates only. For example, the relationship between total flash rate and graupel mass may change in the high graupel density condition of supercell (Allen et al., 2016). The empirical q_g profiles are derived from the model simulation and are therefore sensitive to the model physics schemes (e.g., microphysics schemes) and model setup (e.g., grid spacing). Also, the method would neglect some detailed variation of the vertical distribution of q_g in a specific cloud. This contrasts over using relative humidity or q_v as a proxy for lightning, which does not rely on specific quantitative empirical functional relationship (Fierro et al., 2012).

Further work should be conducted to quantify the impact of the uncertainties of the empirical formulation on forecast performance.

References

Alexander, G. D., Weinman, J. A., Karyampudi, V. M., Olson, W. S., & Lee, A. C. L. (1999). The effect of assimilating rain rates derived from satellites and lightning on forecasts of the 1993 superstorm. *Monthly Weather Review*, *27*(7), 1433–1457.

Allen, B. J., Mansell, E. R., Dowell, D. C., & Deierling, W. (2016). Assimilation of pseudo-GLM data using the ensemble Kalman filter. *Monthly Weather Review*, *144*(9), 3465–3486. https://doi.org/10.1175/mwr-d-16-0117.1

Benjamin, S. G., Dévényi, D., Weygandt, S. S., Brundage, K. J., Brown, J. M., Grell, G. A., … Manikin, G. S. (2004). An hourly assimilation-forecast cycle: The RUC. *Monthly Weather Review*, *132*(2), 495–518. https://doi.org/10.1175/1520-0493(2004)132%3C0495:AHACTR%3E2.0.CO;2

Boccippio, D. J., Cummins, K. L., Christian, H. J., & Goodman, S. J. (2001). Combined satellite-and surface-based estimation of the intracloud-cloud-to-ground lightning ratio over the continental United States. *Monthly Weather Review*, *129*(1), 108–122. https://doi.org/10.1175/1520-0493(2001)129%3C0108:CSASBE%3E2.0.CO;2

Bruning, E. C., Rust, W. D., Schuur, T. J., MacGorman, D. R., Krehbiel, P. R., & Rison, W. (2007). Electrical and polari-metric radar observations of a multicell storm in TELEX. *Monthly Weather Review*, *135*(7), 2525–2544. https://doi.org/10.1175/MWR3421.1

Carey, L. D., Bain, A. L., & Retha, M. (2014). Kinematic and microphysical control of lightning in multicell convection over Alabama during DC3, 23rd Int. Lightning Detection Conf., Tucson, AZ, Vaisala, 20.21 pp.

Chang, D. E., Weinman, J. A., Morales, C. A., & Olson, W. S. (2001). The effect of spaceborne microwave and ground-based continuous lightning measurements on forecasts of the 1998 Groundhog Day storm. *Monthly Weather Review*, *129*(8), 1809–1833. https://doi.org/10.1175/1520-0493(2001)129%3C1809:TEOSMA%3E2.0.CO;2

Chen, F., & Dudhia, J. (2001). Coupling an advanced land surface-hydrology model with the Penn State-NCAR MM5 modeling system, part I: Model implementation and sensitivity. *Monthly Weather Review*, *129*(4), 569–585. https://doi.org/10.1175/1520-0493(2001)129%3C0569:caalsh%3E2.0.co;2

Cheng, W. Y., Liu, Y., Bourgeois, A. J., Wu, Y., & Haupt, S. E. (2017). Short-term wind forecast of a data assimilation/weather forecasting system with wind turbine anemometer measurement assimilation. *Renewable Energy*, *107*, 340–351. https://doi.org/10.1016/j.renene.2017.02.014

Cressman, G. P. (1959). An operational objective analysis system. *Monthly Weather Review*, *87*(10), 367–374.

Deierling, W., Petersen, W. A., Latham, J., Ellis, S., & Christian, H. J. (2008). The relationship between lightning activity and ice fluxes in thunderstorms. *Journal of Geophysical Research*, *113*, D15210. https://doi.org/10.1029/2007JD009700

Dwyer, J. R., Rassoul, H. K., Al-Dayeh, M., Caraway, L., Chrest, A., Wright, B., … Rambo, K. J. (2005). X-ray bursts associated with leader steps in cloud-to-ground lightning. *Geophysical Research Letters*, *32*, L01803. https://doi.org/10.1029/2004GL021782

Ek, M. B., Mitchell, K. E., Lin, Y., Rogers, E., Grunmann, P., Koren, V., … Tarpley, J. D. (2003). Implementation of Noah land surface model advances in the National Centers for Environmental Prediction operational mesoscale Eta model. *Journal of Geophysical Research*, *108*(D22), 8851. https://doi.org/10.1029/2002JD003296

Fierro, A. O., & Reisner, J. M. (2011). High-resolution simulation of the electrification and lightning of Hurricane Rita during the period of rapid intensification. *Journal of the Atmospheric Sciences*, *68*, 477–494. https://doi.org/10.1175/2010JAS3659.1

Fierro, A. O., Gilmore, M. S., Mansell, E. R., Wicker, L. J., & Straka, J. M. (2006). Electrification and lightning in an idealized boundary-crossing supercell simulation of 2 June 1995. *Monthly Weather Review*, *134*(11), 3149–3172. https://doi.org/10.1175/MWR3231.1

Fierro, A. O., Mansell, E. R., Ziegler, C. L., & Macgorman, D. R. (2012). Application of a lightning data assimilation technique in the WRF-ARW model at cloud-resolving scales for the tornado outbreak of 24 May 2011. *Monthly Weather Review*, *140*(8), 2609–2627. https://doi.org/10.1175/mwr-d-11-00299.1

Fierro, A. O., Mansell, E. R., Macgorman, D. R., & Ziegler, C. L. (2013). The implementation of an explicit charging and discharge lightning scheme within the WRF-ARW model: Benchmark simulations of a continental squall line, a tropical cyclone, and a winter storm. *Monthly Weather Review*, *141*(7), 2390–2415. https://doi.org/10.1175/mwr-d-12-00278.1

Fierro, A. O., Gao, J., Ziegler, C. L., Mansell, E. R., MacGorman, D. R., & Dembek, S. R. (2014). Evaluation of a cloud-scale lightning data assimilation technique and a 3DVAR method for the analysis and short-term forecast of the 29 June 2012 Derecho event. *Monthly Weather Review*, *142*(1), 183–202. https://doi.org/10.1175/MWR-D-13-00142.1

Fierro, A. O., Clark, A. J., Mansell, E. R., MacGorman, D. R., Dembek, S. R., & Ziegler, C. L. (2015). Impact of storm-scale lightning data assimilation on WRF-ARW precipitation forecasts during the 2013 warm season over the contiguous United States. *Monthly Weather Review*, *143*(3), 757–777. https://doi.org/10.1175/MWR-D-14-00183.1

Fierro, A. O., Mansell, E. R., Ziegler, C. L., & Macgorman, D. R. (2015). Explicitly simulated electrification and lightning within a tropical cyclone based on the environment of Hurricane Isaac (2012). *Journal of the Atmospheric Sciences*, *72*(11), 4167–4193. https://doi.org/10.1175/jas-d-14-0374.1

Fierro, A. O., Gao, J., Ziegler, C. L., Calhoun, K. M., Mansell, E. R., & Macgorman, D. R. (2016). Assimilation of flash extent data in the variational framework at convection-allowing scales: Proof-of-concept and evaluation for the short-term forecast of the 24 May 2011 tornado out-break. *Monthly Weather Review*, *144*(11), 4373–4393. https://doi.org/10.1175/mwr-d-16-0053.1

Gao, J., & Stensrud, D. J. (2012). Assimilation of reflectivity data in a convective-scale, cycled 3DVAR framework with hydrometeor classifi-cation. *Journal of the Atmospheric Sciences*, *69*(3), 1054–1065. https://doi.org/10.1175/JAS-D-11-0162.1

Gauthier, M. L., Petersen, W. A., Carey, L. D., Carey, L. D., & Christian, H. J. (2006). Relationship between cloud-to-ground lightning and pre-cipitation ice mass: A radar study over Houston. *Geophysical Research Letters*, *33*, L20803. https://doi.org/10.1029/2006GL027244

Goodman, S. J., Blakeslee, R. J., Koshak, W. J., Mach, D., Bailey, J., Buechler, D., … Geoffrey, S. (2013). The GOES-R Geostationary Lightning Mapper (GLM). *Atmospheric Research*, *125-126*, 34–49. https://doi.org/10.1016/j.atmosres.2013.01.006

Grell, G. A., & Freitas, S. R. (2013). A scale and aerosol aware stochastic convective parameterization for weather and air quality modeling. *Atmospheric Chemistry and Physics*, 2014, *13*(9), 23,845–23,893. https://doi.org/10.5194/acpd-13-23845-2013

Grell, G. A., Dudhia, J., & Stauffer, D. R. (1994). *A description of the Fifth-Generation Penn State/NCAR Mesoscale Model (MM5), NCAR/TN-398+STR* (p. 117). Boulder, CO: National Center for Atmospheric Research.

Hong, S.-Y., & Lim, J.-O. J. (2006). The WRF single-moment microphysics scheme (WSM6). *Journal of the Korean Meteorological Society*, *42*, 129–151.

Houze, R. A. (2004). Mesoscale convective systems. *Reviews of Geophysics*, *42*, RG4003. https://doi.org/10.1029/2004RG000150

Hu, M., Xue, M., & Brewster, K. (2006). 3DVAR and cloud analysis with WSR-88D level-II data for the prediction of the Fort Worth, Texas, tornadic thunderstorms. Part I: Cloud analysis and its impact. *Monthly Weather Review*, *134*(2), 675–698. https://doi.org/10.1175/MWR3092.1

Iacono, M. J., Delamere, J. S., Mlawer, E. J., Shephard, M. W., Clough, S. A., & Collins, W. D. (2008). Radiative forcing by long-lived greenhouse gases: Calculations with the AER radiative transfer models. *Journal of Geophysical Research*, *113*, D13103. https://doi.org/10.1029/2008JD009944

Janjić, Z. C. A. I. (1994). The Step-Mountain Eta Coordinate Model: Further developments of the convection, viscous sublayer, and turbulence closure schemes. *Monthly Weather Review*, *122*(5), 927–945. https://doi.org/10.1175/1520-0493(1994)122%3C0927:tsmecm%3E2.0.co;2

Johnson, A., Wang, X., Carley, J. R., Wicker, L. J., & Karstens, C. (2015). A comparison of multiscale GSI-based EnKF and 3DVar data assimilation using radar and conventional observations for midlatitude convective-scale precipitation forecasts. *Monthly Weather Review*, *143*(8), 3087–3108. https://doi.org/10.1175/mwr-d-14-00345.1

Kuhlman, K. M., Ziegler, C. L., Mansell, E. R., MacGorman, D. R., & Straka, J. M. (2006). Numerically simulated electrification and lightning of the 29 June 2000 STEPS supercell storm. *Monthly Weather Review*, *134*(10), 2734–2757. https://doi.org/10.1175/MWR3217.1

Lerach, D. G., Rutledge, S. A., Williams, C. R., & Cifelli, R. (2010). Vertical structure of convective systems during NAME 2004. *Monthly Weather Review*, *138*(5), 1695–1714. https://doi.org/10.1175/2009MWR3053.1

Lin, Y., & Mitchell, K. E. (2005). The NCEP stage II/IV hourly precipitation analyses: Development and applications, 19th Conf. on Hydrology, San Diego, CA, Amer. Meteor. Soc., 1.2. Retrieved from: http://ams.confex.com/ams/ pdfpapers/83847.pdf

Liu, C., & Heckman, S. (2010). The application of total lightning detection and cell tracking for severe weather prediction, TECO-2010-WMO Technical Conf. on Meteor. and Environmental Instruments and Methods of Observation, Helsinki, Finland, WMO. Retrieved from: https://www.wmo.int/pages/prog/www/IMOP/publications/IOM-104_TECO-2010/P2_7_Heckman_USA.pdf

Liu, Y., Bourgeois, A., Warner, T., Swerdlin, S., & Hacker, J. (2005). Implementation of observation-nudging based FDDA into WRF for supporting ATEC test operations, extended abstracts, Joint WRF/MM5 User's Workshop, Boulder, CO, NCAR, 10.7. Retrieved from: http://www2.mmm.ucar.edu/wrf/users/ workshops/WS2005/abstracts/Session10/7-Liu.pdf

Liu, Y., Chen, F., Warner, T., & Basara, J. (2006). Verification of a Mesoscale Data-Assimilation and Forecasting System for the Oklahoma City area during the joint urban 2003 field project. *Journal of Applied Meteorology and Climatology*, *45*(7), 912–929. https://doi.org/10.1175/jam2383.1

Liu, Y., Warner, T. T., Astling, E. G., Bowers, J. F., Davis, C. A., Halvorson, S. F., … Xu, M. (2008). The operational mesogamma-scale analysis and forecast system of the U.S. Army test and evaluation command. Part II: Interrange comparison of the accuracy of model analyses and forecasts. *Journal of Applied Meteorology and Climatology*, *47*(4), 1093–1104. https://doi.org/10.1175/2007jamc1654.1

Liu, Y., Warner, T. T., Bowers, J. F., Carson, L. P., Chen, F., Clough, C. A., … Weingarten, D. S. (2008). The operational mesogamma-scale analysis and forecast system of the U.S. army test and evaluation command. Part I: Overview of the modeling system, the forecast products, and how the products are used. *Journal of Applied Meteorology and Climatology*, *47*(4), 1077–1092. https://doi.org/10.1175/2007jamc1653.1

Lund, N. R., MacGorman, D. R., Schuur, T. J., Biggerstaff, M. I., & Rust, W. D. (2009). Relationships between lightning location and polarimetric radar signatures in a small mesoscale convective system. *Monthly Weather Review*, *137*(12), 4151–4170. https://doi.org/10.1175/2009MWR2860.1

Lynn, B. H. (2017). The usefulness and economic value of total lightning forecasts made with a dynamic lightning scheme coupled with lightning data assimilation. *Weather Forecasting*, *32*(2), 645–663. https://doi.org/10.1175/WAF-D-16-0031.1

Lynn, B. H., Kelman, G., & Ellrod, G. (2015). An evaluation of the efficacy of using observed lightning to improve convective lightning forecasts. *Weather Forecasting*, *30*(2), 405–423. https://doi.org/10.1175/waf-d-13-00028.1

Macgorman, D. R., Rust, W. D., Krehbiel, P., Rison, W., Bruning, E., & Wiens, K. (2005). The electrical structure of two supercell storms during STEPS. *Monthly Weather Review*, *133*(9), 2583–2607. https://doi.org/10.1175/mwr2994.1

Mansell, E. R., MacGorman, D. R., Ziegler, C. L., & Straka, J. M. (2005). Charge structure and lightning sensitivity in a simulated multicell thunderstorm. *Journal of Geophysical Research*, *110*, D12101. https://doi.org/10.1029/2004JD005287

Mansell, E. R. (2010). On sedimentation and advection in multimoment bulk microphysics. *Journal of the Atmospheric Sciences*, *67*(9), 3084–3094. https://doi.org/10.1175/2010JAS3341.1

Mansell, E. R. (2014). Storm-scale ensemble Kalman filter assimilation of total lightning-extent data. *Monthly Weather Review*, *142*(10), 3683–3695. https://doi.org/10.1175/mwr-d-14-00061.1

Mansell, E. R., Ziegler, C. L., & Macgorman, D. R. (2007). A lightning data assimilation technique for mesoscale forecast models. *Monthly Weather Review*, *135*(5), 1732–1748. https://doi.org/10.1175/mwr3387.1

Mansell, E. R., Ziegler, C. L., & Bruning, E. C. (2010). Simulated electrification of a small thunderstorm with two-moment bulk microphysics. *Journal of the Atmospheric Sciences*, *67*(1), 171–194. https://doi.org/10.1175/2009jas2965.1

Marchand, M., & Fuelberg, H. (2014). Assimilation of lightning data using a nudging method involving low-level warming. *Monthly Weather Review*, *142*(12), 4850–4871. https://doi.org/10.1175/MWR-D-14-00076.1

Nag, A., Murphy, M. J., Cummins, K. L., Pifer, A. E., & Cramer, J. A. (2014). Recent evolution of the U.S. National Lightning Detection Network, 23rd Int. Lightning Detection Conf., Tucson, AZ, Vaisala, 6 pp.

Pan, L., Liu, Y., Liu, Y., Li, L., Jiang, Y., Cheng, W., & Roux, G. (2015). Impact of four-dimensional data assimilation (FDDA) on urban climate analysis. *Journal of Advances in Modeling Earth Systems*, *7*(4), 1997–2011. https://doi.org/10.1002/2015ms000487

Papadopoulos, A., Chronis, T. G., & Anagnostou, E. N. (2005). Improving convective precipitation forecasting through assimilation of regional lightning measurements in a mesoscale model. *Monthly Weather Review*, *133*(7), 1961–1977. https://doi.org/10.1175/MWR2957.1

Pessi, A. T., & Businger, S. (2009). Relationships among lightning, precipitation, and hydrometeor characteristics over the North Pacific Ocean. *Journal of Applied Meteorology and Climatology*, *48*(4), 833–848. https://doi.org/10.1175/2008JAMC1817.1

Peters, J. M., & Schumacher, R. S. (2014). Objective categorization of heavy-rain-producing MCS synoptic types by rotated principal component analysis. *Monthly Weather Review*, *142*(5), 1716–1737. https://doi.org/10.1175/MWR-D-13-00295.1

Petersen, W. A., & Rutledge, S. A. (1998). On the relationship between cloud-to-ground lightning and convective rainfall. *Journal of Geophysical Research*, *103*(D12), 14,025–14,040. https://doi.org/10.1029/97JD02064

Petersen, W. A., Christian, H. J., & Rutledge, S. A. (2005). TRMM observations of the global relationship between ice water content and lightning. *Geophysical Research Letters*, *32*, L14819. https://doi.org/10.1029/2005GL023236

Qie, X., Zhu, R., Yuan, T., Wu, X., Li, W., & Liu, D. (2014). Application of total-lightning data assimilation in a mesoscale convective system based on the WRF model. *Atmospheric Research*, *145-146*, 255–266. https://doi.org/10.1016/j.atmosres.2014.04.012

Ribaud, J.-F., Bousquet, O., & Coquillat, S. (2016). Relationships between total lightning activity, microphysics and kinematics during the 24 September 2012 HyMeX bow-echo system. *Quarterly Journal of the Royal Meteorological Society*, *142*, 298–309. https://doi.org/10.1002/qj.2756

Roberts, N. M., & Lean, H. W. (2008). Scale-selective verification of rainfall accumulations from high-resolution forecasts of convective events. *Monthly Weather Review*, *136*(1), 78–97. https://doi.org/10.1175/2007mwr2123.1

Saunders, C. P. R., & Peck, S. L. (1998). Laboratory studies of the influence of the rime accretion rate on charge transfer during crystal/graupel collisions. *Journal of Geophysical Research*, *103*(D12), 13,949–13,956. https://doi.org/10.1029/97JD02644

Sharman, R. D., Liu, Y., Sheu, R.-S., Warner, T. T., Rife, D. L., Bowers, J. F., … Ellison, E. E. (2008). The operational mesogamma-scale analysis and forecast system of the U.S. army test and evaluation command, part III: Forecasting with secondary-applications models. *Journal of Applied Meteorology and Climatology*, *47*(4), 1105–1122. https://doi.org/10.1175/2007jamc1655.1

Stauffer, D. R., & Seaman, N. L. (1990). Use of four-dimensional data assimilation in a limited-area mesoscale model. Part I: Experiments with synoptic-scale data. *Monthly Weather Review*, *118*(6), 1250–1277. https://doi.org/10.1175/1520-0493(1990)118%3C1250:uofdda%3E2.0.co;2

Sun, J., Xue, M., Wilson, J. W., Zawadzki, I., Ballard, S. P., Onvlee-Hooimeyer, J., … Pinto, J. (2014). Use of NWP for nowcasting convective precipitation: Recent progress and challenges. *Bulletin of the American Meteorological Society*, *95*(3), 409–426. https://doi.org/10.1175/bams-d-11-00263.1

Takahashi, T., & Miyawaki, K. (2002). Reexamination of riming electrification in a wind tunnel. *Journal of the Atmospheric Sciences*, *59*(5), 1018–1025. https://doi.org/10.1175/1520-0469(2002)059%3C1018:roreia%3E2.0.co;2

Wiens, K. C., Rutledge, S. A., & Tessendorf, S. A. (2005). The 29 June 2000 supercell observed during STEPS. Part II: Lightning and charge structure. *Journal of the Atmospheric Sciences*, *62*(12), 4151–4177. https://doi.org/10.1175/JAS3615.1

Xue, M., Wang, D., Gao, J., Brewster, K., & Droegemeier, K. K. (2003). The Advanced Regional Prediction System (ARPS), storm-scale numerical weather prediction and data assimilation. *Meteorology and Atmospheric Physics*, *82*(1-4), 139–170. https://doi.org/10.1007/s00703-001-0595-6

Yang, J., Zhang, Z., Wei, C., Lu, F., & Guo, Q. (2017). Introducing the new generation of Chinese geostationary weather satellites—FengYun 4 (FY-4). *Bulletin of the American Meteorological Society*, *98*(8), 1637–1658. https://doi.org/10.1175/BAMS-D-16-0065.1

Zhang, J., Howard, K., Langston, C., Vasiloff, S., Kaney, B., Arthur, A., … Seo, D. J. (2011). National Mosaic and Multi-Sensor QPE (NMQ) system: Description, results, and future plans, *Bulletin of the American Meteorological Society*, *92*(10), 1321–1338.

Ziegler, C. L. (1985). Retrieval of thermal and microphysical variables in observed convective storms. Part 1: Model development and preliminary testing. *Journal of the Atmospheric Sciences*, *42*(14), 1487–1509. https://doi.org/10.1175/1520-0469(1985)042%3C1487:rotamv%3E2.0.co;2